Submitted to ADVANCED MATERIALS

DOI: 10.1002/ ((please add manuscript number))
Article type: Communication

Pb-Sn-Cu Ternary Organometallic Halide Perovskite Solar Cells

Meng Li, Zhao-Kui Wang, Ming-Peng Zhuo, Yun Hu, Ke-Hao Hu, Qing-Qing Ye, Sagar M. Jain, Ying-Guo Yang, Xing-Yu Gao, and Liang-Sheng Liao**

M. Li, Dr. Z. K. Wang, Y. Hu, K. H. Hu, Q. Q. Ye, M. P. Zhuo, Prof. L. S. Liao
Jiangsu Key Laboratory for Carbon-Based Functional Materials & Devices,
Institute of Functional Nano & Soft Materials (FUNSOM),
Soochow University,
Suzhou 215123, China
E-mail: zkwang@suda.edu.cn; lsliao@suda.edu.cn

Dr. Y. G. Yang, Prof. X.Y. Gao
Shanghai Synchrotron Radiation Facility,
Shanghai Institute of Applied Physics, Chinese Academy of Sciences,
Shanghai 201204, China

Dr. S. M. Jain
SPECIFIC, College of Engineering,
Swansea University Bay Campus,
Fabian Way, SA1 8EN Swansea, United Kingdom

Keywords: Perovskite solar cells; Ternary perovskite; Low toxicity: Passivation

Organometallic halide perovskites are a class of charming photovoltaic semiconductors with excellent intrinsic properties such as broad-band absorption, long carrier diffusion length, low cost materials, and solution-processing. [1-3] Remarkable achievements have been obtained for perovskite solar cells (PSCs) with a record power conversion efficiency (PCE) of 22.1%.[4] To date, most high-performance PSCs are relied on lead halides based perovskites. The issue of serious pollution on soil and/or water has to be considered due to the large solubility (K_{sp}) of Pb^{2+} on an order of 1×10^{-8}.[5] And the potential health risks to human beings and significant danger to the ecosystem may reduce the market acceptance of lead based PSCs.[6-9] Seeking lead-free or low-toxic metal halide perovskites that can present similar properties to the lead counterparts is an efficient route to address this challenge. Some low-toxic metal cations, *i.e.* Sn (II), Ge (II), Mn (II), Cu (II), Co (II), In (III), Al (III) and Sb (III), have been utilized to partially substitute Pb in binary metal PSCs.[10-16] Among them, Ge (II) and Mn (II) based alloying perovskites showed extremely low efficiency.[12,13] For Co (II), In (III), and Sb (III), the limited element reserves restrict their commercial applications.[11,15,16] Fortunately, Sn (II) is proven to be an ideal candidate to substitute Pb by their similarity in ionic radii and electronic configuration.[17] And the PCE in Sn based lead-free PSCs has been approached around 6%.[18-22] Nevertheless, the efficiency is still far below that in lead counterpart based devices. Utilizing of alloying perovskite is an efficient route to adjust the absorption wavelength region and improve the device performance. Interestingly, Pb-Sn binary metal perovskites can extend the absorption edge to over 1000 nm. [23,24] With efforts, the device performance of corresponding solar cells has been improved largely with maximum PCE over 15%.[25-29] However, the efficiency is not competing with those Pb-based PSCs. And there is a fact that the efficiency drops systematically with increasing the Sn proportion in the perovskites. The lower PCE is mainly ascribed to the unsatisfied perovskite crystallization due to the easy oxidation from Sn^{2+} to Sn^{4+}. In addition, the poor film quality with worse homogeneity and coverage is another limiting factor on the low-performance of Pb-Sn binary

metal PSCs. Therefore, seeking other low toxic elements and developing novel deposition methods are necessary for fabricating high-performance PSCs.

Herein, we for the first time reported the ternary Pb-Sn-Cu perovskite solar cells by partially replacing of PbI_2 with SnI_2 and $CuBr_2$. A detailed investigation of the effects of Sn^{2+} and Cu^{2+} substitution on the growth and optoelectronic properties of perovskite films was carried out. Sn^{2+} substitution resulted in a red-shift the absorption onset without seriously influencing the absorption property. Cu^{2+} substitution played an important role in improving the perovskite crystallization with large grain size and full coverage by passivating the trap cites at crystal boundaries. Pb-Sn-Cu perovskites exhibited multiple crystal orientations with improved charge transport properties. Consequently, ternary Pb-Sn-Cu PSC exhibited a champion PCE of 21.08% with a V_{OC} of 1.086 V, a short-circuit current density (J_{SC}) of 23.97 mA/cm^2, and a fill factor (FF) of 81% by employing TiO_2 and 2,2',7,7'-tetrakis-(N,N-di-p-methoxyphenylamine)-9,9'-spirobifluorene (Spiro-OMeTAD) as the electron-transporting layer and the hole-transporting layer, respectively.

The precursor solutions of Pb-Sn-Cu ternary perovskite were prepared by mixing methylammonium (MA) iodide, PbI_2, SnI_2 and $CuBr_2$ powders with desired molar ratio in γ-butyrolactone and dimethylsulphoxide (7:3, v/v). The solutions (40 wt%) were stirred overnight at 60 °C and filtered through 0.45 μm filters before film deposition. Pb-Sn-Cu perovskite films were deposited onto the TiO_2 layer based on a two-step spin-coating process in N_2-filled glovebox. A treatment by chlorobenzene drop-casting was executed during the spin-coating process. Pb-Sn-Cu perovskite films could be formed after an annealing at 100 °C for 10 min. **Figure 1**a shows a crystalline structure of $CH_3NH_3Pb_{1-a-b}Sn_aCu_bI_{3-2b}Br_{2b}$ perovskites.

As representatives, **Figure 2**a shows the absorption spectra of $MAPbI_3$, $MAPb_{0.95}Cu_{0.05}I_{0.95}Br_{0.05}$, $MAPb_{0.90}Sn_{0.05}Cu_{0.05}I_{0.95}Br_{0.05}$, $MAPb_{0.85}Sn_{0.10}Cu_{0.05}I_{0.95}Br_{0.05}$, and $MAPb_{0.80}Sn_{0.15}Cu_{0.05}I_{0.95}Br_{0.05}$ perovskite films. with clear absorption onsets. Comparted to

$MAPbI_3$ film, the absorption onset was red-shifted and blue-shifted for $MAPb_{0.95}Sn_{0.05}I_3$ and $Pb_{0.95}Cu_{0.05}I_{2.9}Br_{0.1}$, respectively. The slight change in energy bandgap (E_g) is originated from the part replacement of PbI_2 with SnI_2 or $CuBr_2$.[30-33] For Pb-Sn-Cu ternary perovskite film, there was a slight decrease in E_g from 1.59 eV ($MAPbI_3$) to 1.58 eV ($MAPb_{0.9}Sn_{0.05}Cu_{0.05}I_{2.9}Br_{0.1}$). No large difference in absorption spectra among $MAPbI_3$, $MAPb_{0.95}Sn_{0.05}I_3$, $MAPb_{0.95}Cu_{0.05}I_{2.9}Br_{0.1}$, and $MAPb_{0.9}Sn_{0.05}Cu_{0.05}I_{2.9}Br_{0.1}$ films was observed (Figure S1, Supporting Information). **Figure 2**b shows the X-ray diffraction (XRD) patterns of $MAPbI_3$, $MAPb_{0.95}Sn_{0.05}I_3$ and $MAPb_{0.95}Cu_{0.05}I_{2.9}Br_{0.1}$ binary perovskite, and $MAPb_{0.9}Sn_{0.05}Cu_{0.05}I_{2.9}Br_{0.1}$ ternary perovskite films. A comparison of the diffraction peak intensities corresponding to (110), (220) and (310) crystallographic planes among four samples confirmed the high crystallinity of Pb-Sn-Cu ternary perovskite films. Strong diffraction peaks at 2θ = 14.12°, 28.44°, 31.90°, and several weak diffraction peaks were observed in $MAPbI_3$ sample. After incorporating Sn or Cu to replace Pb, the positions of diffraction peaks were almost unchanged without appearance of new diffraction peaks. However, obvious change of reduced full-width-of-half-maximum (FWHM) and increased diffraction intensity of (110), (220) and (310) diffraction peaks was observed in $MAPb_{0.9}Sn_{0.05}Cu_{0.05}I_{2.9}Br_{0.1}$ ternary perovskite film, indicating a well-preserved crystal structure and the phase purity. This means that the crystallinity was enhanced with enlarged grain size by incorporating Cu^{2+} into Pb-Sn perovskite film. To investigate the atomic composition and electronic structure of the composition of Pb-Sn-Cu ternary perovskite films, X-ray photoemission spectroscopy (XPS) was employed to analyze the core levels of key elements in perovskite layer (**Figure S2**, Supporting Information). **Figure 2**c and d presents the core levels of Cu 2*p* and Sn 3*d* in corresponding perovskite films. No matter in binary perovskite or ternary Pb-Sn-Cu perovskite films, there was no obvious shift for the core levels of Cu 2*p* and Sn 3*d*. This means that Sn and Cu elements have same atomic composition and electronic structure both in binary perovskite and ternary perovskite structures. To evaluate

the element distribution in the perovskite layer, cross-section energy dispersive X-ray (EDX) analysis was carried out (**Figure S3**, Supporting Information). **Figure 2**e and f shows the Pb element in $MAPbI_3$ and Pb, Sn, Cu elements in $MAPb_{0.9}Sn_{0.05}Cu_{0.05}I_{2.9}Br_{0.1}$ based device, respectively. The insets are the corresponding cross-sectional SEM images of the PSCs. Obviously, Sn and Cu elements co-exist with Pb and they distributed homogeneously in the Pb-Sn-Cu perovskite films.

To investigate the effect of Sn and Cu elements on the morphology of perovskite films, scanning electron microscope (SEM) and polarized optical microscopic were used to characterize the film properties. **Figure 3**a-d shows the SEM surface morphologies of $MAPbI_3$, $MAPb_{0.95}Sn_{0.05}I_3$, $MAPb_{0.95}Cu_{0.05}I_{2.9}Br_{0.1}$ and $MAPb_{0.9}Sn_{0.05}Cu_{0.05}I_{2.9}Br_{0.1}$ perovskite films. As shown in **Figure 3**b, the grain size was reduced and the grain boundary became indistinct even if a small amount of Sn substitution (5 mol%). We ascribed it to the different nucleation/growth rate of perovskite film due to the Sn^{2+} incorporation. Furthermore, easy oxidization of Sn^{2+} to Sn^{4+} will cause partial decomposition of perovskite and affect the film morphology with the time going on. [34-36] The instability of Sn-included perovskite films was further confirmed by the polarized optical microscopic evaluation (**Figure S4**, Supporting Information). A large number of crystal branches were observed in $MAPb_{0.95}Sn_{0.05}I_3$ perovskite film, which would affect the film flatness and then the device performance. No obvious aggregation appeared in $MAPbI_3$ and $MAPb_{0.95}Cu_{0.05}I_{2.9}Br_{0.1}$ samples. And the crystallization aggregation was suppressed effectively in $MAPb_{0.9}Sn_{0.05}Cu_{0.05}I_{2.9}Br_{0.1}$ film by a passivation effect of Cu^{2+}. Consequently, partial Cu substitution (5 mol%) resulted in a dense film morphology with enlarged grain size as shown in **Figure 3**c. Particularly, $MAPb_{0.9}Sn_{0.05}Cu_{0.05}I_{2.9}Br_{0.1}$ ternary perovskite possessed excellent film quality with pin-hole free, uniform and large grain size as shown in **Figure 3**d. Br^- may affect the crystal lattice disorder and benefit the perovskite film quality in some cases. In order to clarify the role of Br on the film quality, Cu-excluded perovskite film ($MAPb_{0.95}Sn_{0.05}I_{2.90}Br_{0.10}$) by just using

$PbBr_2$ to replace $CuBr_2$ was preparted. SEM evaluation demonstrated that there was no distinct difference in the crystallization of $MAPb_{0.95}Sn_{0.05}I_{2.90}Br_{0.10}$ and $MAPb_{0.95}Sn_{0.05}I_3$ films (**Figure S5, Supporting Information**). Kim *et al.* also reported that incorporation of Br^- did not no change the crystal size of perovskite film largely.[37] Therefore, in present case, the improved morphology is mainly attributed to the passivation role of Cu^{2+} by minimizing the extrinsic trap sites at the crystal boundaries.[38,39] The incorporation of Cu^{2+} would retard the crystallization process of perovskite film. The decreased growth rate of Pb-Sn-Cu perovskite layer could be reflected from a comparison of photographs of $MAPbI_3$ and $MAPb_{0.9}Sn_{0.05}Cu_{0.05}I_{2.9}Br_{0.1}$ perovskite films during the annealing process (Figure S6, Supporting Information). The slowing down of crystallization process is feasible for forming perovskite film with large grain size. In all, the incorporation of Cu^{2+} could retard the crystallization process of perovskite film and fill up the traps partially, and thus affect the film formation process and the resultant morphology.

To have a deep understanding of electronic structure of Pb-Sn-Cu ternary perovskite, the perovskite film was scraped off and the obtained powder was put onto a copper gird for evaluation. The selected area electron diffraction (SAED) patterns of $MAPbI_3$ and $MAPb_{0.9}Sn_{0.05}Cu_{0.05}I_{2.9}Br_{0.1}$ perovskites are shown in **Figure 3**e and f, respectively. Both samples were found to be composed of some single crystals due to their distinct electron diffraction patterns. **Figure 3**g and h show the transmission electron microscopy (TEM) images of dispersed $MAPbI_3$ and $MAPb_{0.9}Sn_{0.05}Cu_{0.05}I_{2.9}Br_{0.1}$ perovskites scraped from their films. The insets are the corresponding TEM images of individual perovskite particles with the size of micrometer scale. The lattice parameter of $MAPbI_3$ film was determined to be 0.31 nm, which can be indexed by (220) plane of the tetragonal-phase $MAPbI_3$.[40,41] In contrast, $MAPb_{0.9}Sn_{0.05}Cu_{0.05}I_{2.9}Br_{0.1}$ sample have a slightly decreased lattice parameter of 0.30 nm, which is associated with the lattice distortion caused by the smaller atomic radius of Sn and Cu compared with Pb. In addition, no obvious phase separation was observed in

$MAPb_{0.95}Cu_{0.05}I_{2.9}Br_{0.1}$, and $MAPb_{0.9}Sn_{0.05}Cu_{0.05}I_{2.9}Br_{0.1}$ perovskite films even after a treatment of light exposure or thermal treatment (Figure S7, Supporting Information).

Perovskite crystallization mainly determines the photoelectric characteristics and thus the cell performance. To deeply understand the crystalline property, the real-time diffraction data based on a fast 2D area detector combined with a high brightness synchrotron X-ray source was collected. **Figure 4**a-d presents the 2D grazing incidence X-ray diffraction (GIXRD) profiles of $MAPbI_3$, $MAPb_{0.95}Sn_{0.05}I_3$, $MAPb_{0.95}Cu_{0.05}I_{2.9}Br_{0.1}$ and $MAPb_{0.9}Sn_{0.05}Cu_{0.05}I_{2.9}Br_{0.1}$ perovskite film, respectivley. Four GIXRD patterns exhibited strong scattering backgrounds. Comparred to $MAPbI_3$, the presence of strongly scattered secondary spots and rings in $MAPb_{0.9}Sn_{0.05}Cu_{0.05}I_{2.9}Br_{0.1}$ perovskite indicates that the crystalline domains possessed good orientation relative to the substrate plane. **Figure 4**e shows the azimuthally integrated scattering intensity of corresponding GIXRD patterns of two perovskite samples along the ring at q = 10 nm^{-1}, where q is the scattering vector ($q = 4\pi \sin(\theta)/\lambda$). Besides the sharp peak at the azimuth angle of 90°, preferential orientation with obvious peaks at the azimuth angles of 40° (180°-40°) was observed in $MAPb_{0.9}Sn_{0.05}Cu_{0.05}I_{2.9}Br_{0.1}$ perovskite film. This means that there are different stacking ways for the grain crystals in $MAPb_{0.9}Sn_{0.05}Cu_{0.05}I_{2.9}Br_{0.1}$ perovskite. The multiple ordered crystal orientations would result in efficient charge transport in Pb-Sn-Cu ternary perovskite film. Hole- and electron-dominated devices were further fabricated to evaluate the carrier behavior in Pb-only and Pb-Sn-Cu perovskite films. Based on the space charge limited current (SCLC) extrapolation, the hole mobility and electron mobility in $MAPb_{0.9}Sn_{0.05}Cu_{0.05}I_{2.9}Br_{0.1}$ perovskite film was extrapolated to be 1.20 $cm^2\ V^{-1}\ s^{-1}$ and 0.83 $cm^2\ V^{-1}\ s^{-1}$, respectively, which are obviously higher than that of 0.73 $cm^2\ V^{-1}\ s^{-1}$ and 0.67 $cm^2\ V^{-1}\ s^{-1}$ in $MAPbI_3$ (Figure S8, Table S1, Supporting Information). The improved charge transport characteristics in the Pb-Sn-Cu ternary perovskite film will be befeficial for the cell performance. To investigate the Sn and Cu effect on the extrinsic trap sites and defect energy distribution in the perovskite films, thermal admittance spectroscopy

measurements was carried out to evaluate the trap density of states (tDOS) in $MAPbI_3$, $MAPb_{0.95}Sn_{0.05}I_3$, $MAPb_{0.95}Cu_{0.05}I_{2.9}Br_{0.1}$, and $MAPb_{0.9}Sn_{0.05}Cu_{0.05}I_{2.9}Br_{0.1}$ based solar cells. As shown in **Figure 4**f, $MAPb_{0.95}Sn_{0.05}I_3$ based sample demonstrated the highest trap density among four samples. After incorporting Cu^{2+}, trap densities were reduced at the shallow trap region between 0.25 and 0.35 eV compared with $MAPbI_3$ based sample. These are direct evidence for the the passivation effect of Cu^{2+} on the perovskite film.

To investigate the device performance of Pb-Sn-Cu ternary perovskite based solar cells, planar n-i-p structure PSCs with a structure of FTO/TiO_2/$MAPb_{1-a-b}Sn_aCu_bI_{3-2b}Br_{2b}$/spiro-OMeTAD/$MoO_3$/Ag were fabricated as shown in **Figure 1**b. TiO_2 and spiro-OMeTAD was used as the electron- and the hole- transport layer, respectively. TiO_2 compact layer was coated on the FTO substrates by soaking in titanium tetrachloride precursor solution and depositing in an pre-heated oven. Spiro-OMeTAD layer was depostied on perovskite light absorption layer by spin-coating using bis(trifluoromethylsulfonyl)-imide lithium salt (Li-TFSI) (acetonitrile) and 4-tert-butylpyridine (tBP) as the dopants. **Figure 1**c shows a typical cross-section scanning electron microscopy (SEM) image of Pb-Sn-Cu ternary perovskite based PSCs. **Figure 5**a shows the *J-V* characteristics of $MAPbI_3$, $MAPb_{0.95}Sn_{0.05}I_3$, $MAPb_{0.95}Cu_{0.05}I_{2.9}Br_{0.1}$ and $MAPb_{0.9}Sn_{0.05}Cu_{0.05}I_{2.9}Br_{0.1}$ based PSCs under AM 1.5G illumination with the light intensity of 100 mW cm^{-2}. The key cell parameters are summarized in **Table 1**. $MAPbI_3$ based reference device presents a PCE of 17.89% with a J_{SC} of 22.18 mA cm^{-2}, a V_{OC} of 1.07 V, and an FF of 0.75. The device casted from Pb-Sn binary perovskite shows an obviously decreased PCE of 16.76% when 5 mol% of Pb was substituted by Sn. The lowered PCE is attributed to the decreased *V*oc. In contrast, Pb-Cu binary perovskite based device exhibits an enhanced PCE of 19.02% with a J_{SC} of 22.81 mA cm^{-2}, a V_{OC} of 1.13 V, and an FF of 0.74. The optimization of varied substitution ratio of Cu^{2+} and Sn^{2+} indicated that excessive incorporations (> 5 mol%) of Cu^{2+} and Sn^{2+} would deteriorate the device performance seriously (Figure S9, Table S2, Supporting Information). As shown in **Table 1**,

partial substitution of Sn and Cu can improve the *J*sc [32] and the *V*oc [33], respectively. And the pinhole-free Pb-Sn-Cu perovskite film with large grain size is beneficial for obtaining a high FF. With optimization, $MAPb_{0.9}Sn_{0.05}Cu_{0.05}I_{2.9}Br_{0.1}$ perovskite based solar cell presented the best performance with a PCE of 21.08%, J_{SC} of 23.97 mA cm^{-2}, V_{OC} of 1.086 V, and FF of 81% as shown in **Figure 5**b. The reproducibility of the device performance was evaluated by characterizing over 30 cells. The histograms of the PCE parameters displayed in **Figure 5**c verified the reproducibility of high efficiency in $MAPb_{0.9}Sn_{0.05}Cu_{0.05}I_{2.9}Br_{0.1}$ based PSCs. **Figure 5**d shows the steady-state photocurrent and efficiency measured at the maximum power point (0.88 V). The PCE of the $MAPb_{0.9}Sn_{0.05}Cu_{0.05}I_{2.9}Br_{0.1}$ based device stabilizes at 19.89%, which is close to the PCE obtained from the reverse scan *J-V* measurement. The incident-photon-to-current efficiency (IPCE) spectra of $MAPbI_3$ and $MAPb_{0.9}Sn_{0.05}Cu_{0.05}I_{2.9}Br_{0.1}$ based devices are displayed in **Figure 5**e. Improved external quantum efficiency was observed in 450-800 nm range in Pb-Sn-Cu perovskite based device, which is coincided with the similar band edge of the corresponding absorption spectra (**Figure S10,** Supporting Information). The photocurrent densities integrated from IPCE spectra of $MAPbI_3$ and $MAPb_{0.9}Sn_{0.05}Cu_{0.05}I_{2.9}Br_{0.1}$ based PSCs was 21.69 $mAcm^{-2}$ and 23.25 mA cm^{-2}, respectively, which were well matched with the J_{SC} obtained in *J-V* curves. Furthermore, the photocurrent hysteresis phenomenon in two devices was evaluated by recording the *J-V* curves with forward and reverse scan directions as shown in **Figure 5**f. $MAPbI_3$ based reference device showed large current hysteresis, leading to a difference between the PCE of 16.32% (forward scan) and the PCE of 17.89% (reverse scan) (**Table S3**, Supporting Information). $MAPb_{0.9}Sn_{0.05}Cu_{0.05}I_{2.9}Br_{0.1}$ based device presented a reduction in the current hysteresis. The PCE of 20.24% in reverse scan direction was close to the 21.08% in the forward scan direction. The statistical PCE distribution and current hysteresis in $MAPb_{0.95}Cu_{0.05}I_{2.9}Br_{0.1}$ and $MAPb_{0.95}Sn_{0.05}I_3$ based devices were also provided for comparison (Figure S11, Figure S12, Table S3, Supporting Information).

The photocurrent hysteresis is associated with the traps sites, ferroelectricity, and ion migration in the perovskite films. In present case, Cu^{2+} doping can passivate the Pb-Sn-Cu perovskite films with reduced defects or charge trap sites, resulting in a suppression of the photocurrent hysteresis. The passivation role of Cu^{2+} was further verified in the PSCs with large Sn substitution ratio. Even if at 15 mol% Sn^{2+} substitution, Pb-Sn-Cu perovskite based device still can keep a PCE as high as 16.45% (**Figure S13, Table S4** Supporting Information). In addition, a preliminary stability study revealed that Pb-Sn based device demonstrated the worst stability. By incorporting suitable Cu^{2+}, the cell stability could be improved at some extent (Figure S14, Supporting Information). Deep investigation on the stabilities among these devices will be studies in the future.

In summary, we have developed highly efficient Pb-Sn-Cu ternary perovskite solar cells for the first time by partially replacing of PbI_2 with SnI_2 and $CuBr_2$. The roles of Sn and Cu substitution of Pb have been investigated to deposit high quality Pb-Sn-Cu perovskite films with full film coverage and large grain size. Sn^{2+} substitution resulted in a red-shift of the absorption onset, whereas worsen the film quality. Cu^{2+} substitution played an important role in improving the morphology and crystallization of Sn-included alloying perovskites by passivating the trap cites at the crystal boundaries. Consequently, a high efficiency (21.08%) inverted planar Pb-Sn-Cu ternary metal perovskite solar cell was obtained. This work opens a new route to fabricate high efficiency Pb-Sn alloying perovskite solar cells by Cu^{2+} passivation.

Experimental Section

Materials and Solution Preparation: Methylamine (24 mL, 33 wt% in absolute ethanol), hydroiodic acid (10 mL, 57 wt% in water), titanium tetrachloride, Lithium

bis(trifluoromethanesulfonyl)imide (Li-TFSI) and 4-tert-butyl pyridine (*t*BP) were purchased from Sigma-Aldrich. Lead iodide (PbI_2, 99.999%), tin iodide (SnI_2, 99.99%), copper bromide ($CuBr_2$, 99.99%), dimethyl sulfoxide, γ-butyrolactone and chlorobenzene were obtained from Alfa Aesar Ltd. Spiro-OMeTAD were purchased from 1-Material Ltd. CH_3NH_3I precursor was synthesized and purified by following previously reported process.[42] TiO_2 precursor solution was prepared by the reported method.[43] Perovskite precursor solution was prepared by mixing 1 mol PbI_2 and 1 mol MX_2 (PbI_2, SnI_2, $CuBr_2$) powder with a molar ration of 1:1 in 1 mL γ-butyrolactone and dimethylsulphoxide (7:3, v/v) with stirring overnight at 60 °C. Spiro-OMeTAD solution was prepared by mixing 22 μL TFSI-Li solution (520 mg Li-TFSI in 1 *m*L acetonitrile) and 36 μL 4-tert-butylpyridine with 90 *m*g spiro-OMeTAD in 1 *m*L chlorobenzene solution.

Device Fabrication: The FTO substrates with a sheet resistance of ~15Ω/sq were thoroughly cleaned with acetone, ethanol, and deionized water for sequence in ultrasonic bath for 15 min, respectively. And then the substrates were immersed into 200 *m*L $TiCl_4$ solution at 70 °C for 1h. Subsequently, the perovskite solution was then spin-coated onto the TiO_2 layer by a consecutive two-step spin-coating process at 1000 and 4000 rpm for 20 and 40 s, respectively. During the second spin-coating step, the substrate was treated with a chlorobenzene drop-casting. Then the perovskite substrate was heated at 100 °C for 10 min in nitrogen glovebox. After annealing, the spiro-OMeTAD solution was coated onto the perovskite layer at 5000 rpm/40 s. Finally, the device was transferred to a vacuum chamber under 2×10^{-6} Torr for MoO_3 and Ag electrode evaporation. MoO_3 (8 nm) and Ag (100 nm) was subsequently vacuum-evaporated at a rate of 0.2 Å/s and 3 Å/s, respectively. The active area of each device is 9 mm^2 defined through a shadow mask.

Characterization: Current density-voltage characteristics of perovskite solar cells under 1 sun illumination were performed using a programmable Keithley 2400 source meter under AM 1.5G solar irradiation at 100 mW cm^{-2} (Newport, Class AAA solar simulator, 94023A-U).

All the devices were tested under simulated xenon light with an intensity of 100 mW cm^2, and *J–V* curves measured with the sweep delay time was 100 ms. And light intensity was calibrated by a standard silicon solar cell 91150. The incident-photon-to-current efficiency (IPCE) measurement was performed using a system combining a xenon lamp, a monochromator, a chopper and a lock-in amplifier together with a calibrated silicon photodetector. The absorbance of the HTLs films were measured with an UV/Vis spectrophotometer (PerkinElmer Lambda 750). Atomic force microscopy (AFM) images were obtained using a Veeco Multimode V instrument to evaluate the surface morphology of films in tapping mode. The field-emission scanning electron microscope (SEM) images were obtained from a Quanta 200 FEG. The grazing incidence X-ray diffraction (GIXRD) measurements were performed at the BL14B1 beamline of the Shanghai Synchrotron Radiation Facility (SSRF) using X-ray with a wavelength of 1.24 Å. Two-dimensional (2D) GIXRD patterns were acquired by a MarCCD mounted vertically at a distance ~223 mm from the sample with a grazing incidence angle of 0.2º and an exposure time of 20 sec. The 2D GIXRD patterns were analyzed using the FIT2D software and displayed in scattering vector q coordinates. XPS measurements were carried out using a monochromatic Al Kα source (1486.6 eV) in a Kratos AXIS Ultra-DLD ultrahigh vacuum surface analysis system.

Supporting Information

Supporting Information is available from the Wiley Online Library or from the authors.

Acknowledgements

The authors acknowledge financial support from the National Key R&D Program of China (No. 2016YFA0202400), the Natural Science Foundation of China (No. 61674109), and the Natural Science Foundation of Jiangsu Province (No. BK20170059). This project is also funded by the Collaborative Innovation Center of Suzhou Nano Science and Technology, and

by the Priority Academic Program Development of Jiangsu Higher Education Institutions (PAPD).

Received: ((will be filled in by the editorial staff))
Revised: ((will be filled in by the editorial staff))
Published online: ((will be filled in by the editorial staff))

References

[1] A. Kojima, K. Teshima, Y. Shirai, T. Miyasaka, *J. Am. Chem. Soc.* **2009**, *131*, 6050.

[2] S. D. Stranks, G. E. Eperon, G. Grancini, C. Menelaou, M. J. Alcocer, T. Leijtens, L. M. Herz, A. Petrozza, H. J. Snaith, *Science* **2013**, *342*, 341.

[3] D. Bi, W. Tress, M. I. Dar, P. Gao, J. Luo, C. Renevier, K. Schenk, A. Abate, F. Giordano, J.-P. C. Baena, *Science adv.* **2016**, *2*, e1501170.

[4] NREL Best Research Cell Efficiencies, http://www.nrel.gov/pv/ assets/images/efficiency-chart.png, (accessed: January 2017).

[5] P. Patnaik, Handbook of inorganic chemicals; McGraw-Hill New York **2003**.

[6] L. Qiu, J. Deng, X. Lu, Z. Yang, H. Peng, *Angew. Chem. Int. Ed*. **2014**, *53*, 10425.

[7] M. Grätzel, *Nature Mater.* **2014**, *13*, 838.

[8] M. Lyu, J. H. Yun, P. Chen, M. Hao, L. Wang, *Adv. Energy Mater.* **2017**, *7*, 1602512.

[9] Z. Shi, J. Guo, Y. Chen, Q. Li, Y. Pan, H. Zhang, Y. Xia, W. Huang, *Adv. Mater.* **2017**, *29*, 160005.

[10] D. B. Mitzi, C. Feild, Z. Schlesinger, R. Laibowitz, *J. Solid State Chem*. **1995**, *114*, 159.

[11] D. B. Mitzi, K. Liang, *Chem. Mater.* **1997**, *9*, 2990.

[12] H. Arend, W. Huber, F. Mischgofsky, G. Richter-van Leeuwen, *J. Cryst. Growth* **1978**, *43*, 213.

[13] Y. Ohishi, T. Oku, A. Suzuki, *AIP Conf. Proc*., **2016,** *1709*, 020020.

[14] M. T. Klug, A. Osherov, A. A. Haghighirad, S. D. Stranks, P. R. Brown, S. Bai, J. T.-W. Wang, X. Dang, V. Bulović, H. J. Snaith, *Energy Environ. Sci*. **2017**, *10*, 236.

[15] P. Singh, P. J. S. Rana, P. Dhingra, P. Kar, *J. Mater. Chem. C* **2016**, *4*, 3101.

[16] P.-P. Sun, Q.-S. Li, S. Feng, Z.-S. Li, *Phys. Chem. Chem. Phys.* **2016**, *18*, 14408.

[17] E. Mosconi, P. Umari, F. De Angelis, *J. Mater. Chem. A* **2015**, *3*, 9208.

[18] F. Hao, C. C. Stoumpos, D. H. Cao, R. P. Chang, M. G. Kanatzidis, *Nature Photon.* **2014**, *8*, 489.

[19] N. K. Noel, S. D. Stranks, A. Abate, C. Wehrenfennig, S. Guarnera, A.-A. Haghighirad, A. Sadhanala, G. E. Eperon, S. K. Pathak, M. B. Johnston, *Energy Environ. Sci*. **2014**, *7*, 3061.

[20] W. Liao, D. Zhao, Y. Yu, C. R. Grice, C. Wang, A. J. Cimaroli, P. Schulz, W. Meng, K. Zhu, R. G. Xiong, *Adv. Mater.* **2016**, *28*, 9333.

[21] F. Hao, C. C. Stoumpos, P. Guo, N. Zhou, T. J. Marks, R. P. Chang, M. G. Kanatzidis, *J. Am. Chem. Soc.* **2015**, *137*, 11445.

[22] M. Konstantakou, T. Stergiopoulos, *J. Mater. Chem. A* **2017**, *5*, 11518.

[23] F. Hao, C. C. Stoumpos, R. P. Chang, M. G. Kanatzidis, *J. Am. Chem. Soc.***2014**, *136*, 8094.

[24] Y. Ogomi, A. Morita, S. Tsukamoto, T. Saitho, N. Fujikawa, Q. Shen, T. Toyoda, K. Yoshino, S. S. Pandey, T. Ma, *J. phys. Chem. lett.* **2014**, *5*, 1004.

[25] F. Zuo, S. T. Williams, P. W. Liang, C. C. Chueh, C. Y. Liao, A. K. Y. Jen, *Adv. Mater.* **2014**, *26*, 6454.

[26] Z. Yang, A. Rajagopal, C. C. Chueh, S. B. Jo, B. Liu, T. Zhao, A. K. Y. Jen, *Adv. Mater.* **2016**, *28*, 8990.

[27] W. Liao, D. Zhao, Y. Yu, N. Shrestha, K. Ghimire, C. R. Grice, C. Wang, Y. Xiao, A. J. Cimaroli, R. J. Ellingson, *J. Am. Chem. Soc.* **2016**, *138*, 12360.

[28] H. L. Zhu, J. Xiao, J. Mao, H. Zhang, Y. Zhao, W. C. Choy, *Adv. Funct. Mater*. **2017**, *27*, 1605469.

[29] Y. Li, W. Sun, W. Yan, S. Ye, H. Rao, H. Peng, Z. Zhao, Z. Bian, Z. Liu, H. Zhou, *Adv. Energy Mater.* **2016**, *6*, 1601353.

[30] Y. Kim, Z. Yang, A. Jain, O. Voznyy, G. H. Kim, M. Liu, L. N. Quan, F. P. García de Arquer, R. Comin, J. Z. Fan, *Angew. Chem. Int. Ed*. **2016**, *55*, 9586.

[31] E. T. McClure, M. R. Ball, W. Windl, P. M. Woodward, *Chem. Mater*. **2016**, *28*, 1348.

[32] D. Cortecchia, H. A. Dewi, J. Yin, A. Bruno, S. Chen, T. Baikie, P. P. Boix, M. Grätzel, S. Mhaisalkar, C. Soci, *Inorg. Chem*. **2016**, *55*, 1044.

[33] R. S. Sanchez, V. Gonzalez-Pedro, J.-W. Lee, N.-G. Park, Y. S. Kang, I. Mora-Sero, J. Bisquert, *J. phys. chem. lett.* **2014**, *5*, 2357.

[34] M. A. Green, A. Ho-Baillie, H. J. Snaith, *Nature Photon.* **2014**, *8*, 506.

[35] M. H. Kumar, S. Dharani, W. L. Leong, P. P. Boix, R. R. Prabhakar, T. Baikie, C. Shi, H. Ding, R. Ramesh, M. Asta, *Adv. Mater.* **2014**, *26*, 7122.

[36] T. Yokoyama, D. H. Cao, C. C. Stoumpos, T.-B. Song, Y. Sato, S. Aramaki, M. G. Kanatzidis, *J. phys. Chem. Lett*. **2016**, *7*, 776.

[37] M. C. Kim, B. J. Kim, D. Y. Son, N. G. Park, H. S. Jung, and M. Choi, *Nano Lett.*, **2016**, *16*, 5756

[38] M. Abdi‐Jalebi, M. I. Dar, A. Sadhanala, S. P. Senanayak, M. Franckevičius, N. Arora, Y. Hu, M. K. Nazeeruddin, S. M. Zakeeruddin, M. Grätzel, *Adv. Energy Mater*. **2016**, *6*, 1502472.

[39] M. Jahandar, J. H. Heo, C. E. Song, K.-J. Kong, W. S. Shin, J.-C. Lee, S. H. Im, S.-J. Moon, *Nano Energy* **2016**, *27*, 330.

[40] D.-Y. Son, J.-W. Lee, Y. J. Choi, I.-H. Jang, S. Lee, P. J. Yoo, H. Shin, N. Ahn, M. Choi, D. Kim, *Nature Energy* **2016**, *1*, 16081.

[41] S. Kim, S. Bae, S.-W. Lee, K. Cho, K. D. Lee, H. Kim, S. Park, G. Kwon, S.-W. Ahn, H.-M. Lee, *Sci. Rep*. **2017**, *7*, 1200.

[42] Z. K. Wang, M. Li, Y. G. Yang, Y. Hu, H. Ma, X. Y. Gao, L. S. Liao, *Adv. Mater*. **2016**, *28*, 6695.

[43] A. Yella, L.-P. Heiniger, P. Gao, M. K. Nazeeruddin, M. Grätzel, *Nano lett.* **2014**, *14*, 2591.

Sub

Figures and Tables

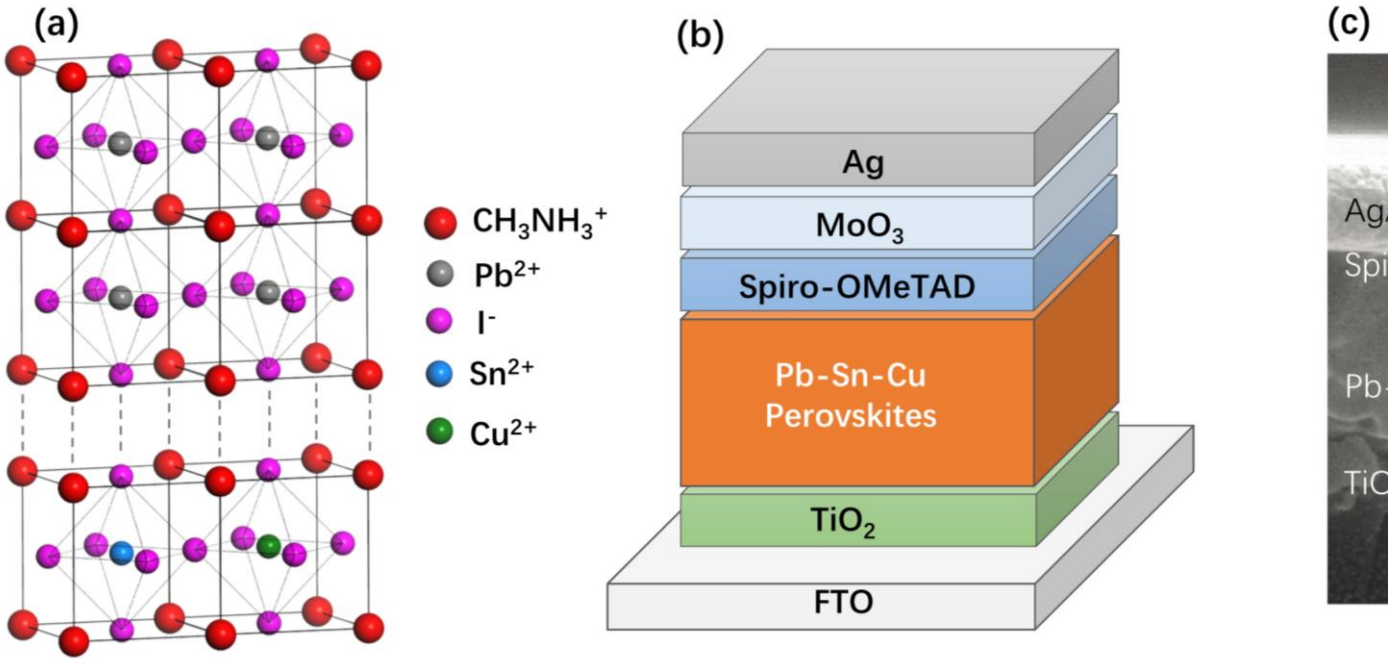

Figure 1 a) An illustration of the molecule structure of $CH_3NH_3Pb_{1-a-b}Sn_aCu_bI_{3-2b}Br_{2b}$ perovskite. b) Dev
perovskite based solar cells. c) Cross-sectional SEM image of Pb-Sn-Cu ternary perovskite based solar cells wi
Cu perovskite/Spiro-OMeTAD/MoO_3/Ag.

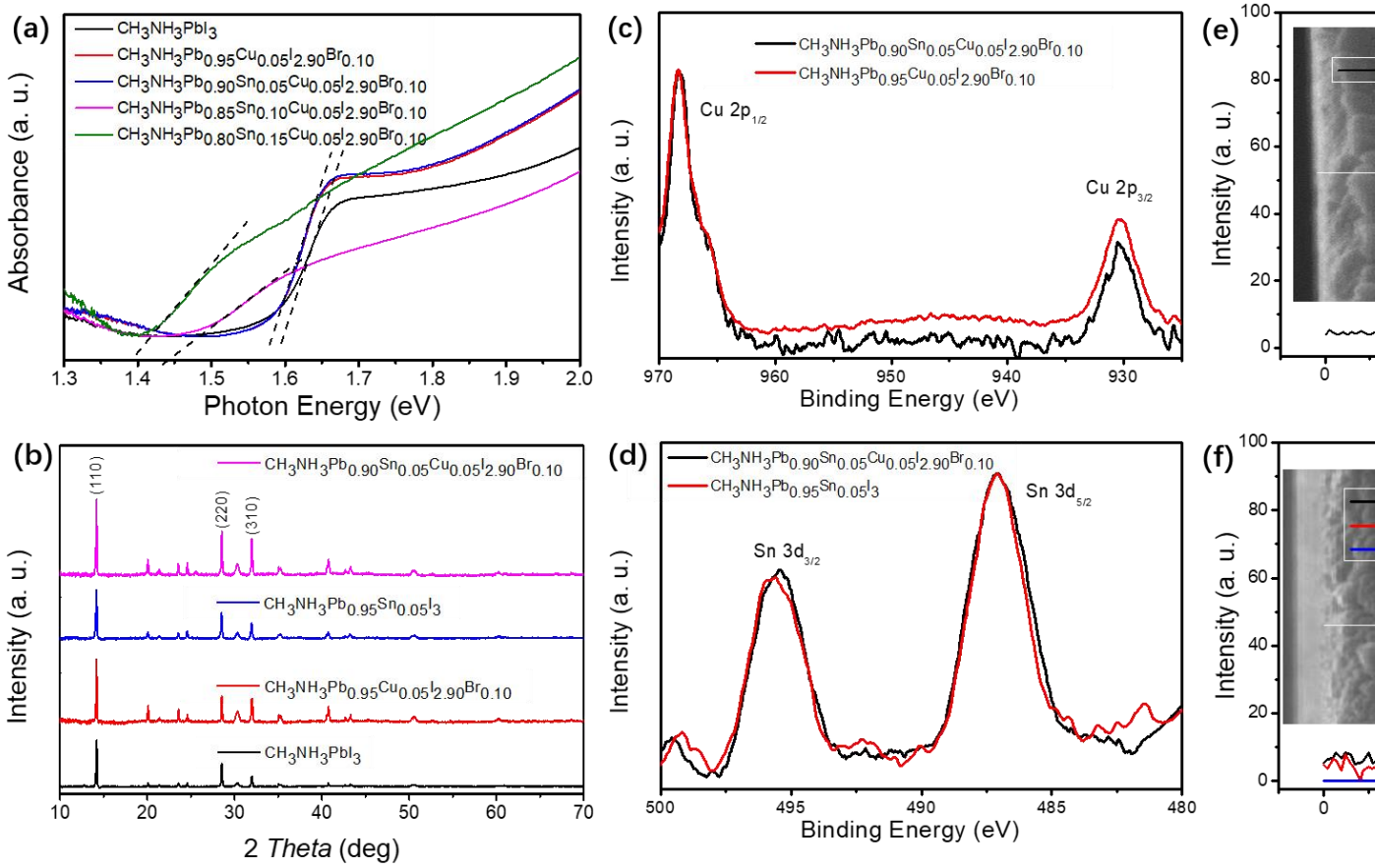

Figure 2 a) Absorption spectra and b) XRD spectra of $MAPbI_3$, $MAPb_{0.95}Cu_{0.05}I_{0.95}Br_0$ $MAPb_{0.85}Sn_{0.10}Cu_{0.05}I_{0.95}Br_{0.05}$, and $MAPb_{0.80}Sn_{0.15}Cu_{0.05}I_{0.95}Br_{0.05}$ perovskite films. c) Cu 2p core-level XPS sp $MAPb_{0.9}Sn_{0.05}Cu_{0.05}I_{2.9}Br_{0.1}$ perovskite films. d) Sn 3d core-level XPS spectra of $MAPb_{0.95}Sn_{0.05}I_3$ and $MAPb_{0.9}$ EDX analysis of e) Pb element in $MAPbI_3$ and f) Pb, Sn, Cu elements in $MAPb_{0.9}Sn_{0.05}Cu_{0.05}I_{2.9}Br_{0.1}$ based PSCs sectional SEM images.

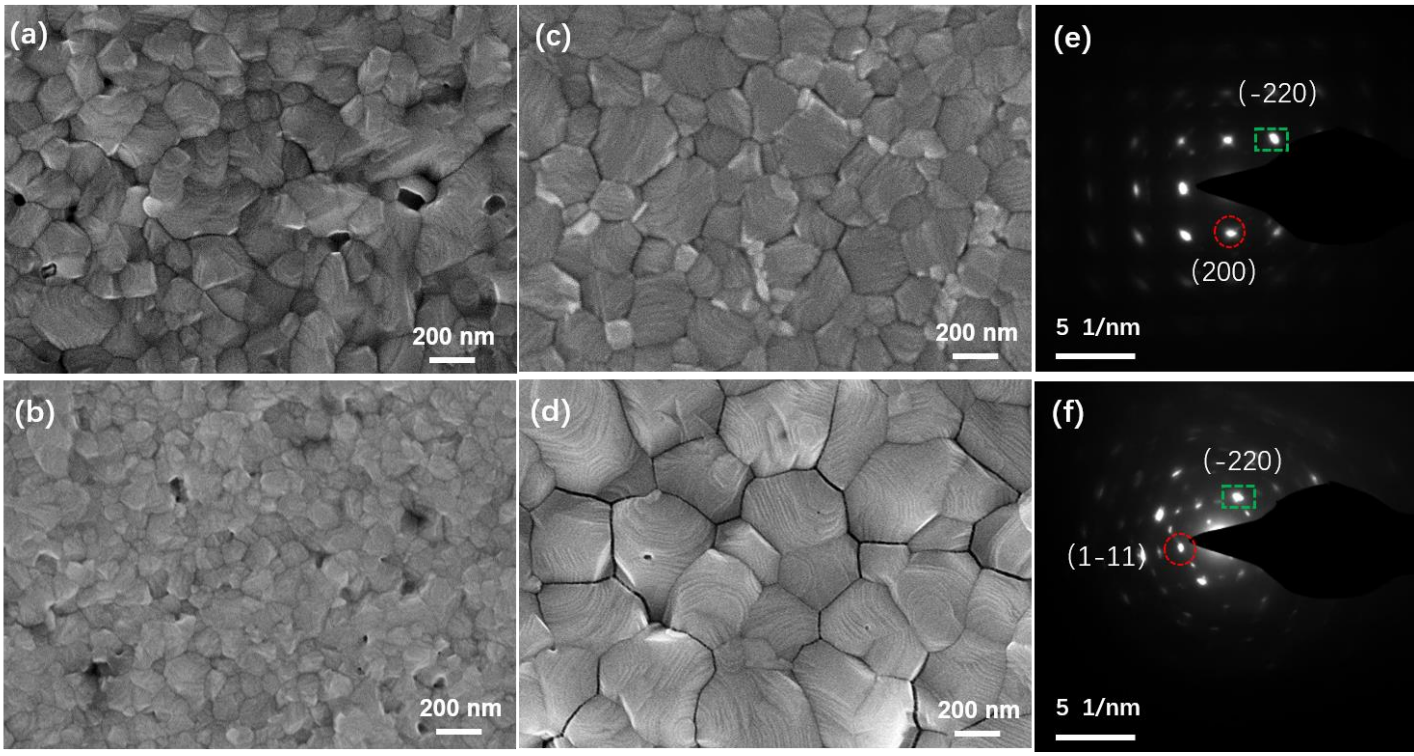

Figure 3 Top SEM images of a) $MAPbI_3$, b) $MAPb_{0.95}Sn_{0.05}I_3$, c) $MAPb_{0.95}Cu_{0.05}I_{2.9}Br_{0.1}$, and d) $MAPb_{0.9}S$ SAED pattern of e) $MAPbI_3$ and f) $MAPb_{0.9}Sn_{0.05}Cu_{0.05}I_{2.9}Br_{0.1}$. TEM images of g) $MAPbI_3$ and h) $MAPb_{0.9}Sn_{0}$ images of corresponding perovskite particles.

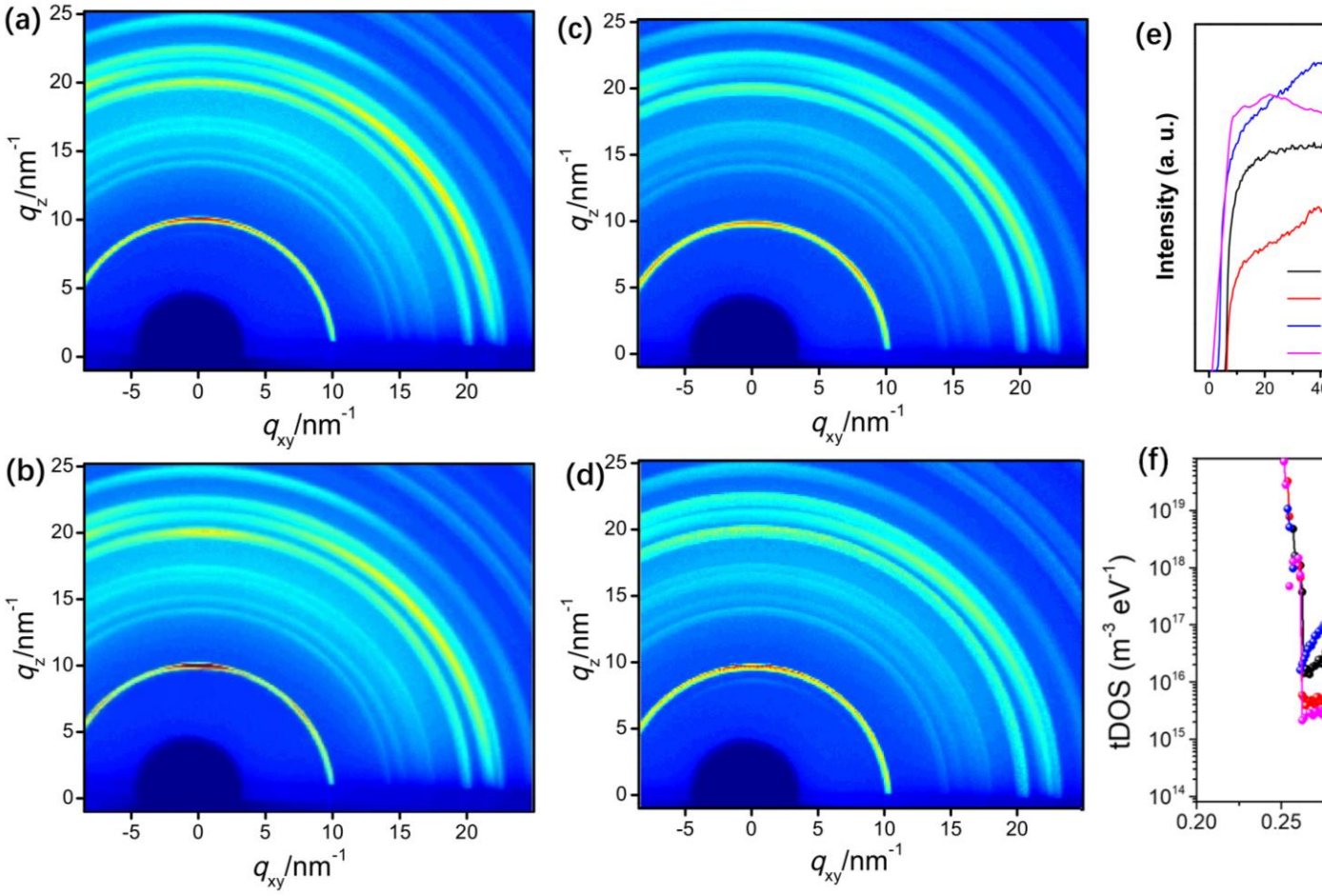

Figure 4 GIXRD patters of a) $MAPbI_3$, b) $MAPb_{0.95}Sn_{0.05}I_3$, c) $MAPb_{0.95}Cu_{0.05}I_{2.9}Br_{0.1}$, and d) $MAPb_{0.9}Sn_{0}$ Radially integrated intensity plots along the ring at q = 10 nm^{-1}, assigned to the (110) plane of $MAPbI_3$, MAP and $MAPb_{0.9}Sn_{0.05}Cu_{0.05}I_{2.9}Br_{0.1}$ perovskite films. f) Trap density of states (tDOS) in $MAPbI_3$, $MAPb_{0.95}S$ $MAPb_{0.9}Sn_{0.05}Cu_{0.05}I_{2.9}Br_{0.1}$ based perovskite solar cells.

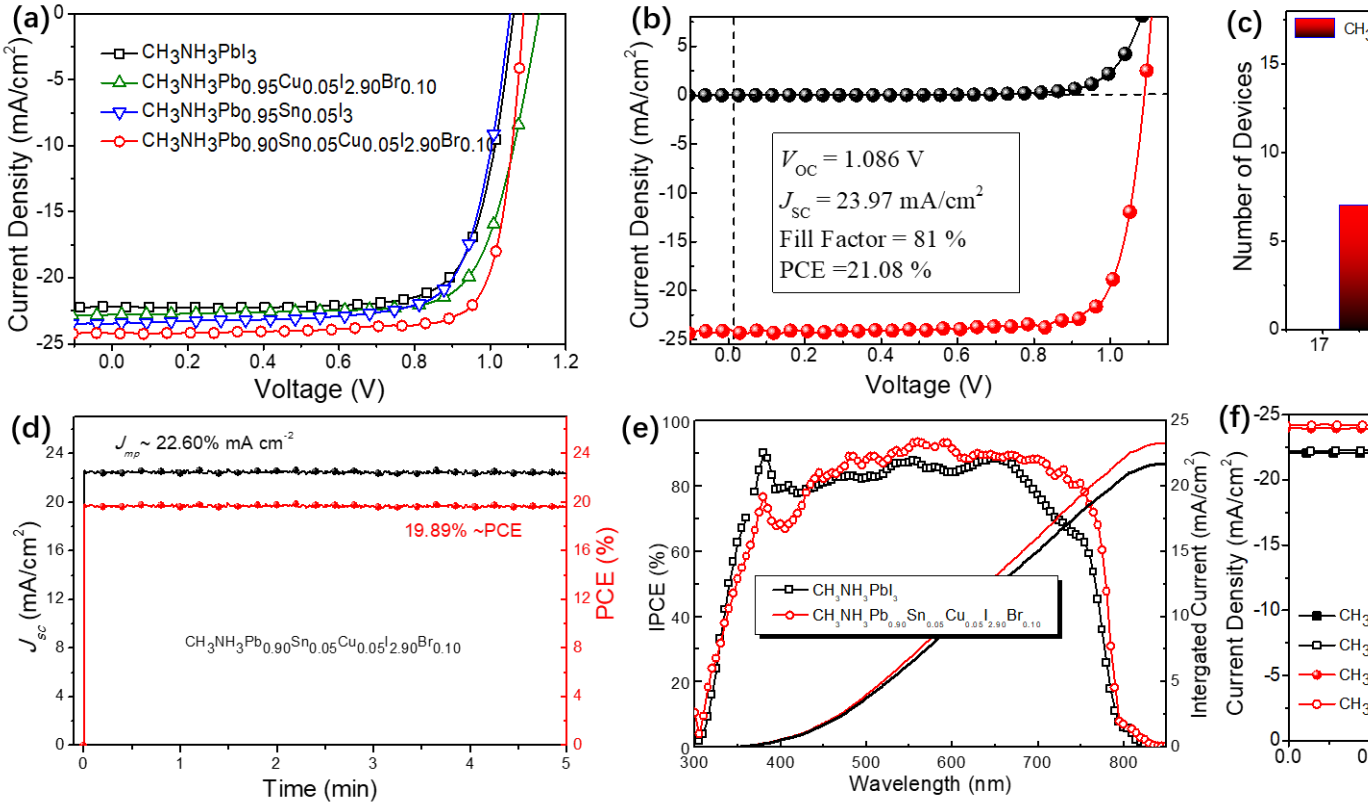

Figure 5 a) *J-V* curves of perovskite solar cells measured under simulated AM 1.5 sunlight of 100 mW cm^{-2}. b under AM 1.5G illumination of 100 mW cm^{-2} and in the dark. c) A histogram of PCEs meas $MAPb_{0.9}Sn_{0.05}Cu_{0.05}I_{2.9}Br_{0.1}$ based perovskite solar cells. d) Maximal steady-state photocurrent output a $MAPb_{0.9}Sn_{0.05}Cu_{0.05}I_{2.9}Br_{0.1}$ based device at 0.88 V and their corresponding power output. e) IPCE sp $MAPb_{0.9}Sn_{0.05}Cu_{0.05}I_{2.9}Br_{0.1}$ based perovskite solar cells. f) *J-V* curves of $MAPbI_3$ and $MAPb_{0.9}Sn_{0.05}Cu_{0.05}$ scanned in forward and reverse directions.

Table 1. Cell parameters of perovskite solar cells with $MAPbI_3$, $MAPb_{0.95}Sn_{0.05}I_3$, $MAPb_{0.95}Cu_{0.05}I_{2.9}Br_{0.1}$ and $MAPb_{0.9}Sn_{0.05}Cu_{0.05}I_{2.9}Br_{0.1}$ as the active layer.

Perovskite Layer	J_{SC} (mA cm^{-2})	V_{OC} (V)	FF	PCE (%)
$MAPbI_3$	22.18	1.07	0.75	17.89
$MAPb_{0.95}Cu_{0.05}I_{2.9}Br_{0.1}$	22.81	1.13	0.74	19.02
$MAPb_{0.95}Sn_{0.05}I_3$	23.28	1.06	0.68	16.76
$MAPb_{0.9}Sn_{0.05}Cu_{0.05}I_{2.9}Br_{0.1}$	23.97	1.08	0.81	21.08

Table of Content:

Pb-Sn-Cu ternary perovskite solar cells were fabricated by partially replacing of PbI_2 with SnI_2 and $CuBr_2$. Sn^{2+} substitution resulted in a red-shift of the absorption onset, whereas worsen the film quality. Cu^{2+} substitution paved a route to passivate the trap cites at the crystal boundaries. As a result, a maximum power conversion efficiency of 21.08% was achieved with improved cell stabiilty.

Keywords: Perovskite solar cells; Ternary perovskite; Low toxicity: Passivation

By *Meng Li, Zhao-Kui Wang*, Ming-Peng Zhuo, Yun Hu, Ke-Hao Hu, Qing-Qing Ye, Sagar M. Jain, Ying-Guo Yang, Xing-Yu Gao, and Liang-Sheng Liao**

Title: **Pb-Sn-Cu Ternary Organometallic Halide Perovskite Solar Cells**

ToC figure ((Please choose one size: 55 mm broad × 50 mm high or 110 mm broad × 20 mm high. Please do not use any other dimensions))

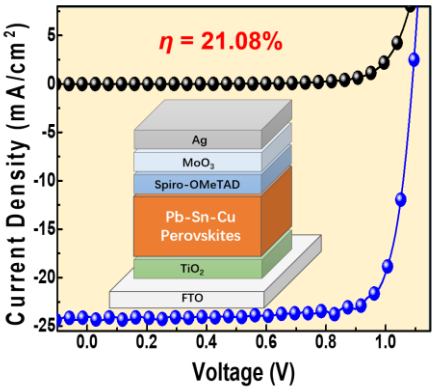

((Supporting Information can be included here using this template))

Supporting Information

Pb-Sn-Cu Ternary Organometallic Halide Perovskite Solar Cells

Meng Li, Zhao-Kui Wang, Ming-Peng Zhuo, Yun Hu, Ke-Hao Hu, Qing-Qing Ye, Sagar M. Jain, Ying-Guo Yang, Xing-Yu Gao, and Liang-Sheng Liao**

M. Li, Dr. Z. K. Wang, Y. Hu, K. H. Hu, Q. Q. Ye, M. P. Zhuo, Prof. L. S. Liao
Jiangsu Key Laboratory for Carbon-Based Functional Materials & Devices,
Institute of Functional Nano & Soft Materials (FUNSOM),
Soochow University,
Suzhou 215123, China
E-mail: zkwang@suda.edu.cn; lsliao@suda.edu.cn

Dr. Y. G. Yang, Prof. X.Y. Gao
Shanghai Synchrotron Radiation Facility,
Shanghai Institute of Applied Physics, Chinese Academy of Sciences,
Shanghai 201204, China

Dr. S. M. Jain
SPECIFIC, College of Engineering,
Swansea University Bay Campus,
Fabian Way, SA1 8EN Swansea, United Kingdom

Keywords: Perovskite solar cells; Ternary perovskite; Low toxicity: Passivation

Table of Contents

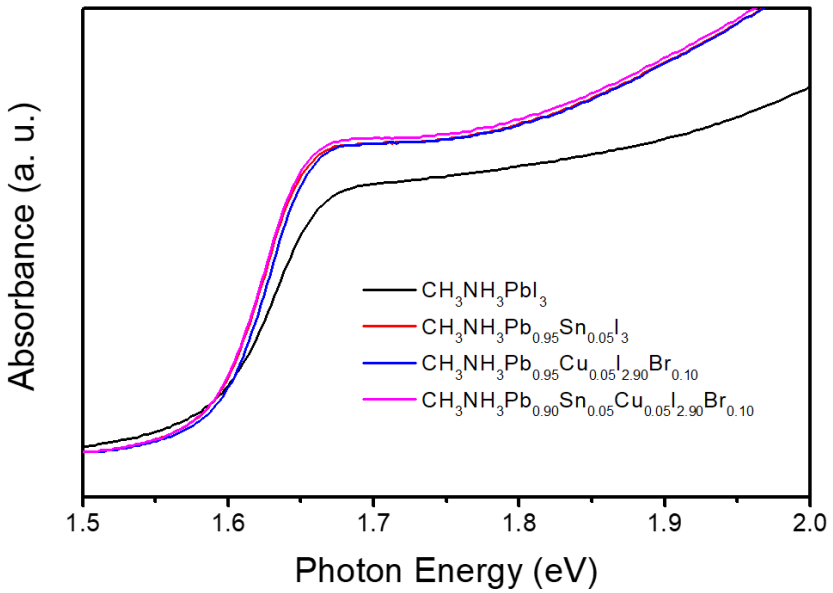

Figure S1. Absorption spectra of $MAPbI_3$, $MAPb_{0.95}Sn_{0.05}I_3$, $MAPb_{0.95}Cu_{0.05}I_{2.9}Br_{0.1}$, and $MAPb_{0.9}Sn_{0.05}Cu_{0.05}I_{2.9}Br_{0.1}$ perovskite films.

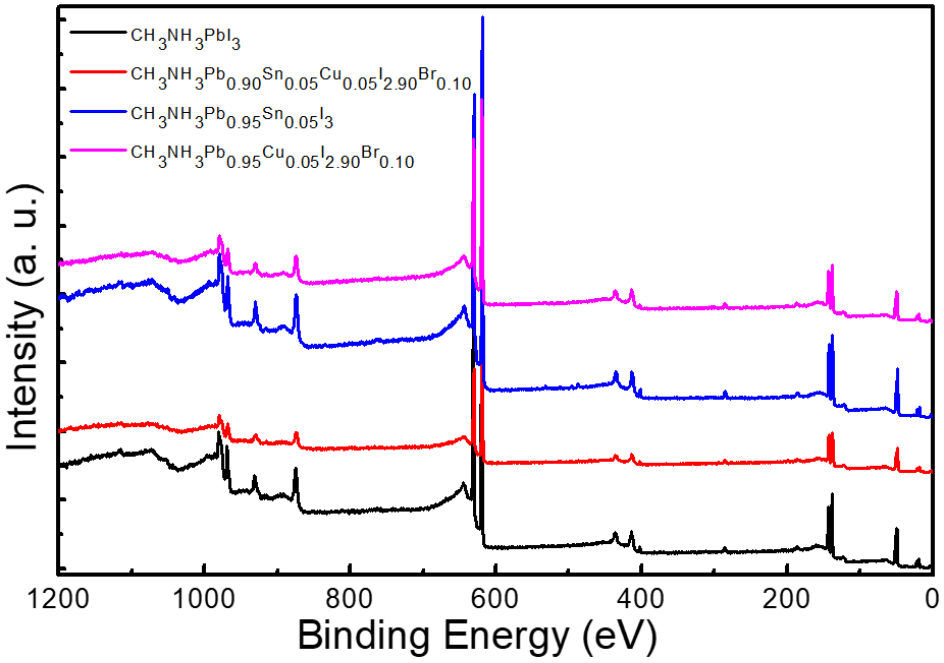

Figure S2. Full scan of XPS spectra of $MAPb_{1-a-b}Sn_aCu_bI_{3-2b}Br_{2b}$ perovskite films.

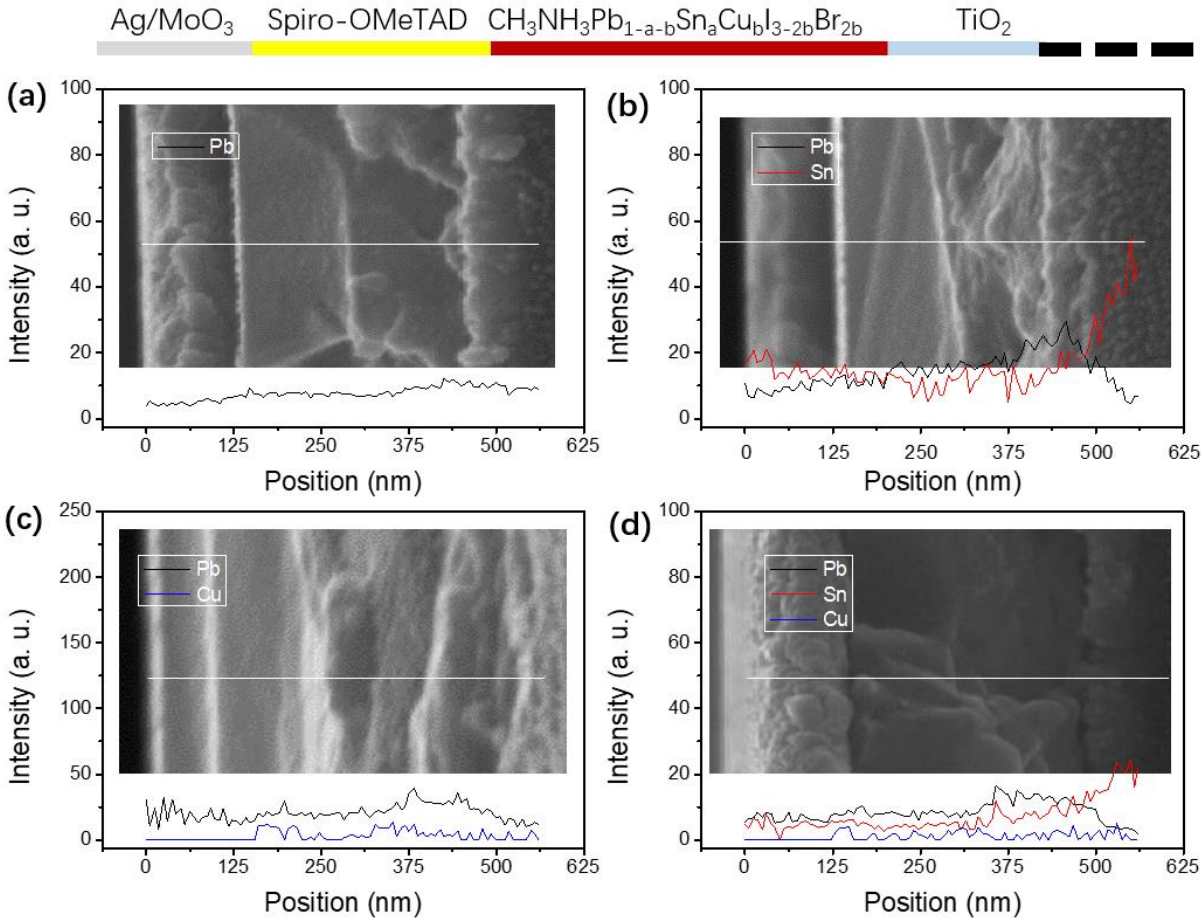

Figure S3. EDX line maps for lead, tin and copper in (a) $MAPbI_3$, (b) $MAPb_{0.95}Sn_{0.05}I_3$, (c) $MAPb_{0.95}Cu_{0.05}I_{2.9}Br_{0.1}$, (d) $MAPb_{0.9}Sn_{0.05}Cu_{0.05}I_{2.9}Br_{0.1}$ Based PSCs. Insets are the SEM images showing cross-sectional views of the PSCs.

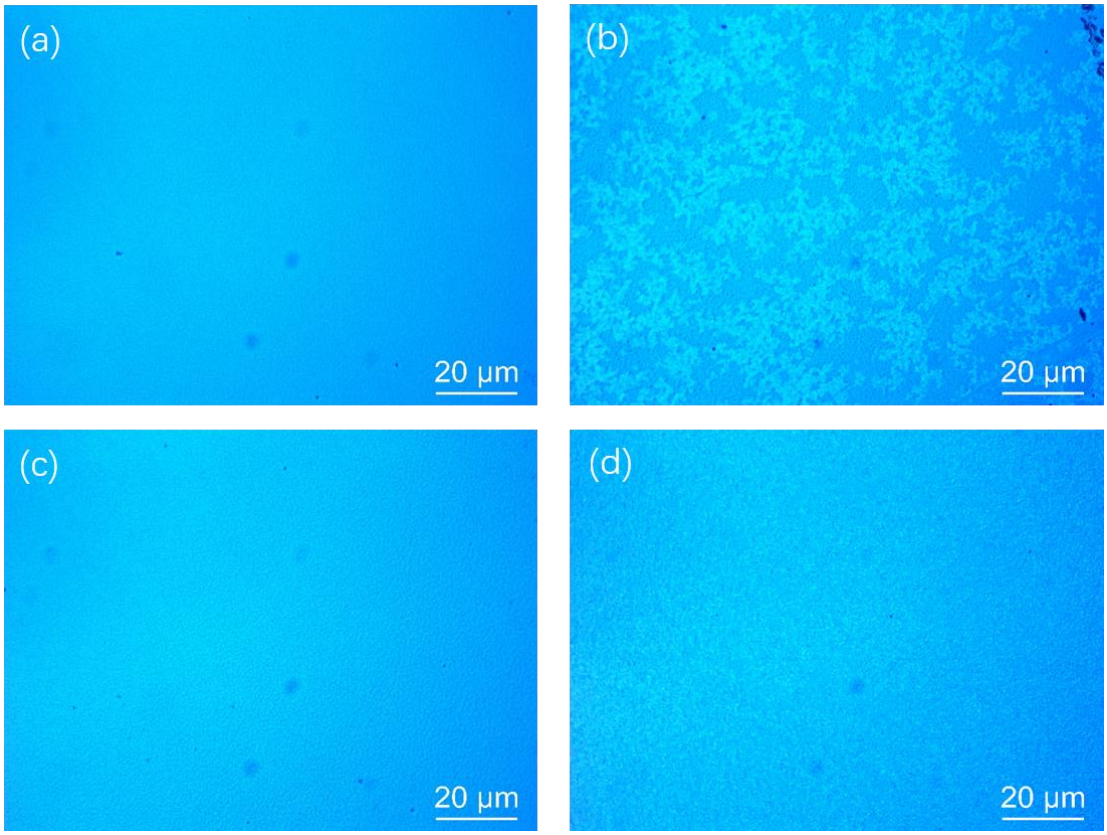

Figure S4. Polarized optical microscopic surface images of (a) $MAPbI_3$, (b) $MAPb_{0.95}Sn_{0.05}I_3$, (c) $MAPb_{0.95}Cu_{0.05}I_{2.9}Br_{0.1}$ and (d) $MAPb_{0.9}Sn_{0.05}Cu_{0.05}I_{2.9}Br_{0.1}$ perovskite films.

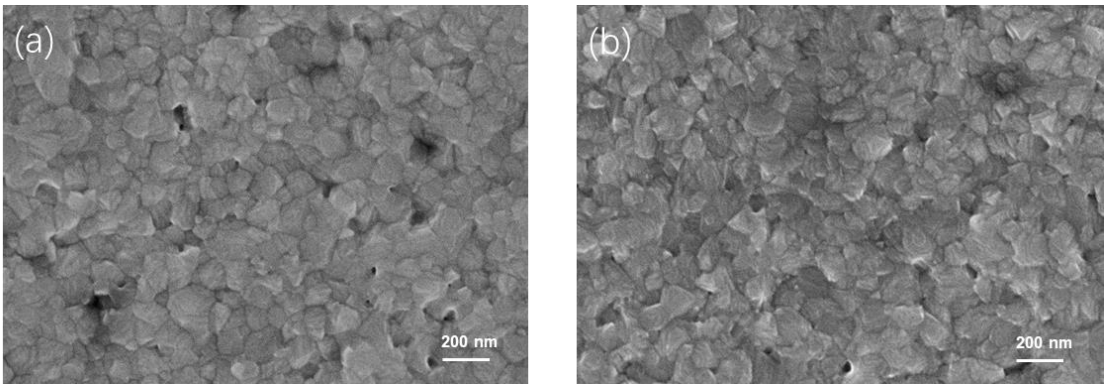

Figure S5. SEM images of (a) $MAPb_{0.95}Sn_{0.05}I_3$ and (b) $MAPb_{0.95}Sn_{0.05}I_{2.90}Br_{0.10}$ perovskite films on FTO/TiO_2 underlayers.

Figure S6. Taken photographs of $MAPbI_3$, $MAPb_{0.95}Sn_{0.05}I_3$, and $MAPb_{0.9}Sn_{0.05}Cu_{0.05}I_{2.9}Br_{0.1}$ perovskite films during annealing and crystallization process.

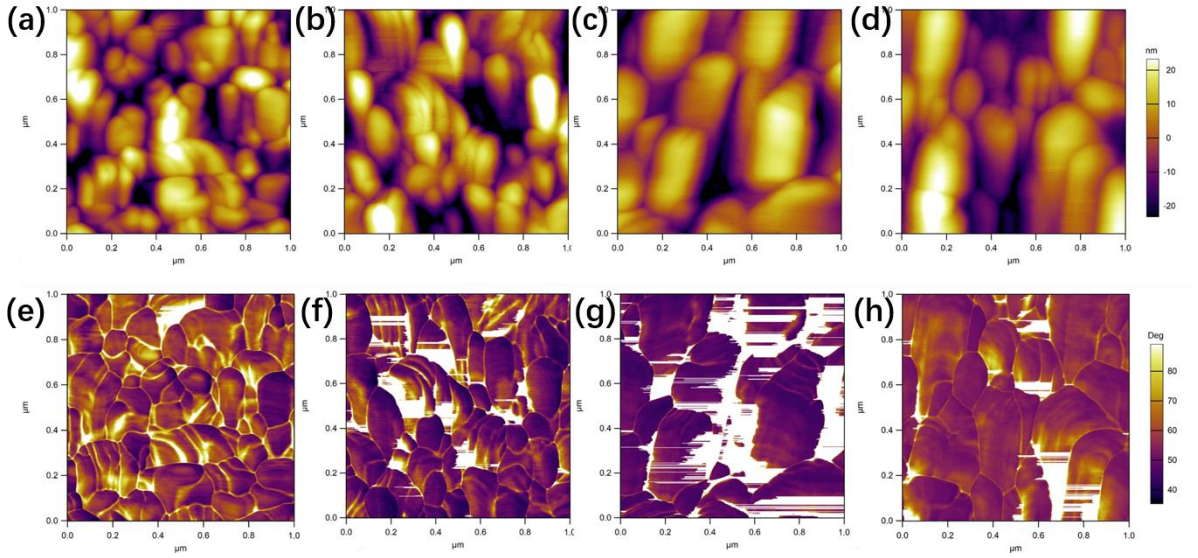

Figure S7. AFM height (a, b, c, d) and phase images(e, f, g, h) of $MAPbI_3$, $MAPb_{0.95}Sn_{0.05}I_3$, $MAPb_{0.95}Cu_{0.05}I_{2.9}Br_{0.1}$, and $MAPb_{0.9}Sn_{0.05}Cu_{0.05}I_{2.9}Br_{0.1}$ perovskite films.

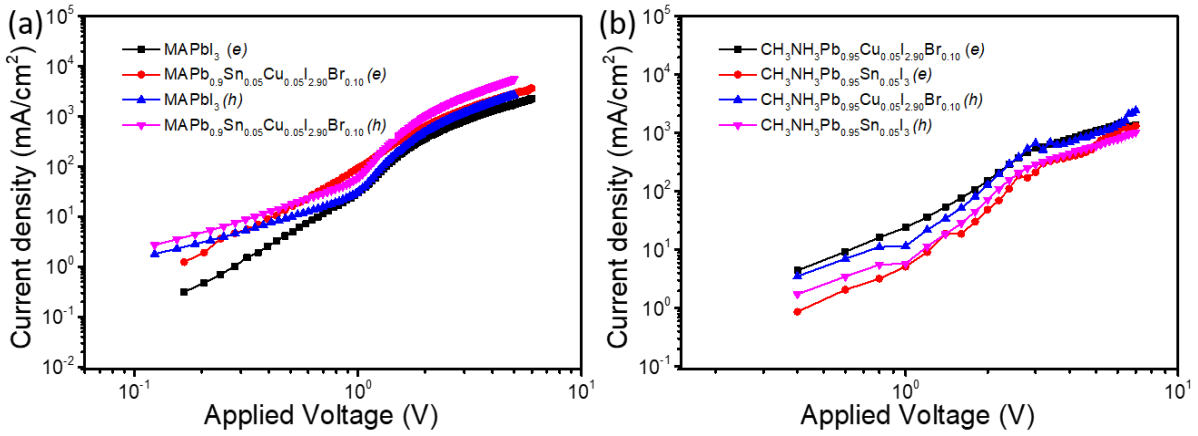

Figure S8. *J-V* characteristics of $MAPbI_3$, $MAPb_{0.95}Sn_{0.05}I_3$, $MAPb_{0.95}Cu_{0.05}I_{2.9}Br_{0.1}$, and $MAPb_{0.9}Sn_{0.05}Cu_{0.05}I_{2.9}Br_{0.1}$ perovskite based hole-dominated and electron-dominated devices.

Table S1 The hole mobility and electron mobility of $MAPbI_3$, $MAPb_{0.95}Sn_{0.05}I_3$, $MAPb_{0.95}Cu_{0.05}I_{2.9}Br_{0.1}$, and $MAPb_{0.9}Sn_{0.05}Cu_{0.05}I_{2.9}Br_{0.1}$ perovskite films.

	Hole mobility ($cm^2V^{-1}s^{-1}$)	**Electronic mobility ($cm^2V^{-1}s^{-1}$)**
$MAPbI_3$	0.731	0.672
$MAPb_{0.85}Sn_{0.05}Cu_{0.05}I_{2.90}Br_{0.10}$	1.202	0.825
$MAPb_{0.95}Sn_{0.05}I_3$	0.501	0.536
$MAPb_{0.95}Cu_{0.05}I_{2.90}Br_{0.10}$	0.926	0.759

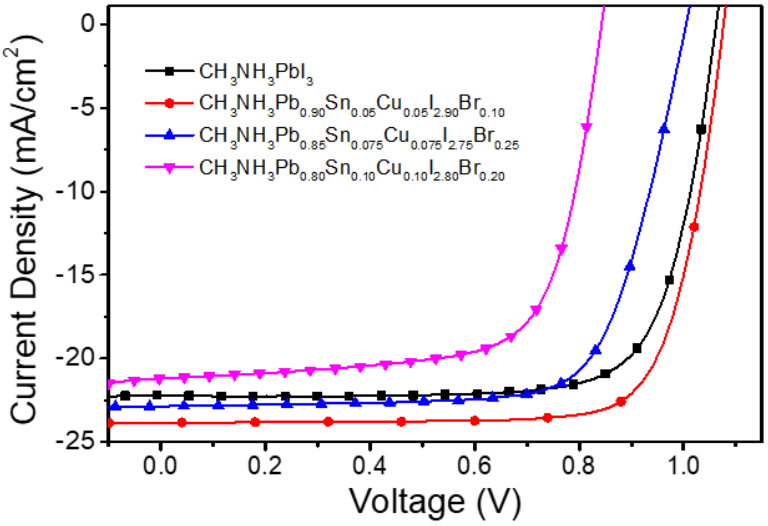

Figure S9. *J-V* curves of dependent device performance of perovskite solar cells on the different ratios of Cu^{2+} and Sn^{2+} measured under simulated AM 1.5 sunlight of 100 mW cm^{-2}.

Table S2. Cell parameters of perovskite solar cells with $CH_3NH_3PbI_3$, $CH_3NH_3Pb_{0.90}Sn_{0.05}Cu_{0.05}I_{2.90}Br_{0.10}$, $CH_3NH_3Pb_{0.85}Sn_{0.075}Cu_{0.075}I_{2.75}Br_{0.25}$ and $CH_3NH_3Pb_{0.80}Sn_{0.10}Cu_{0.10}I_{2.80}Br_{0.20}$ as the active layer.

Perovskite layer	J_{SC}	V_{OC} (V)	FF	PCE (%)
$CH_3NH_3PbI_3$	22.18	1.07	0.75	17.89
$CH_3NH_3Pb_{0.90}Sn_{0.05}Cu_{0.05}I_{2.90}Br_{0.10}$	23.97	1.08	0.81	21.08
$CH_3NH_3Pb_{0.85}Sn_{0.075}Cu_{0.075}I_{2.75}Br_{0.2}$	22.85	1.01	0.72	16.58
$CH_3NH_3Pb_{0.80}Sn_{0.10}Cu_{0.10}I_{2.80}Br_{0.20}$	21.19	0.84	0.70	12.53

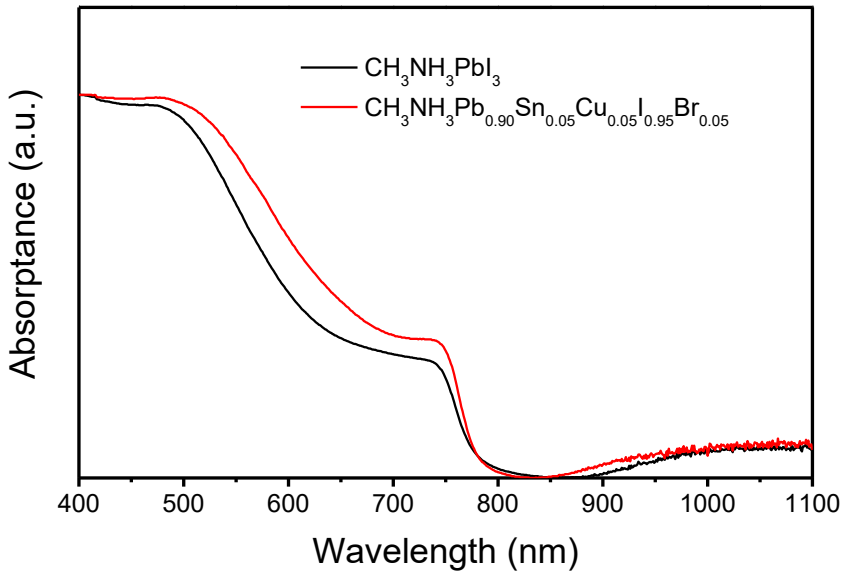

Figure S10. Absorption spectra of $MAPbI_3$ and $MAPb_{0.9}Sn_{0.05}Cu_{0.05}I_{2.9}Br_{0.1}$ perovskite films deposited on TiO_2 layer.

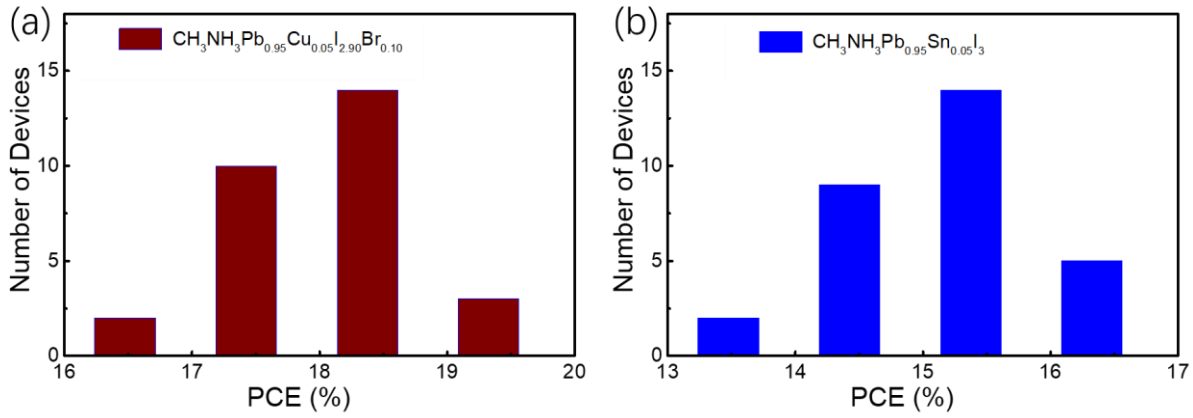

Figure S11. Histogram of PCEs measured from (a) $MAPb_{0.95}Cu_{0.05}I_{2.9}Br_{0.1}$ and (b) $MAPb_{0.95}Sn_{0.05}I_3$ based perovskite solar cells.

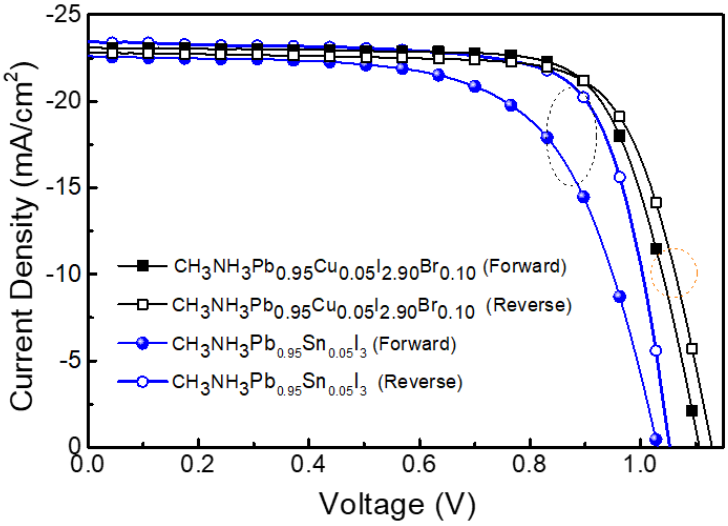

Figure S12. *J-V* curves of $MAPb_{0.95}Cu_{0.05}I_{2.9}Br_{0.1}$ and $MAPb_{0.95}Sn_{0.05}I_3$ based perovskite solar cells scanned in forward and reverse directions.

Table S3. Cell parameters of $MAPbI_3$, $MAPb_{0.95}Cu_{0.05}I_{2.90}Br_{0.10}$, $MAPb_{0.95}Sn_{0.05}I_3$ and $MAPb_{0.9}Sn_{0.05}Cu_{0.05}I_{2.9}Br_{0.1}$ based PSCs scanned in forward and reverse directions.

Perovskite Layer	J_{SC} (mA cm^{-2})	V_{OC} (V)	FF	PCE (%)
$MAPbI_3$ Forward	22.08	1.02	0.73	16.32
$MAPbI_3$ Reverse	22.18	1.07	0.75	17.89
$MAPb_{0.95}Cu_{0.05}I_{2.90}Br_{0.10}$ Forward	23.08	1.11	0.74	18.97
$MAPb_{0.95}Cu_{0.05}I_{2.90}Br_{0.10}$ Reverse	22.81	1.13	0.74	19.02
$MAPb_{0.95}Sn_{0.05}I_3$ Forward	22.59	1.04	0.65	15.17
$MAPb_{0.95}Sn_{0.05}I_3$ Reverse	23.28	1.06	0.68	16.76
$MAPb_{0.90}Cu_{0.05}Sn_{0.05}I_{2.90}Br_{0.10}$ Forward	23.73	1.08	0.80	20.24
$MAPb_{0.90}Cu_{0.05}Sn_{0.05}I_{2.90}Br_{0.10}$ Reverse	23.97	1.08	0.81	21.08

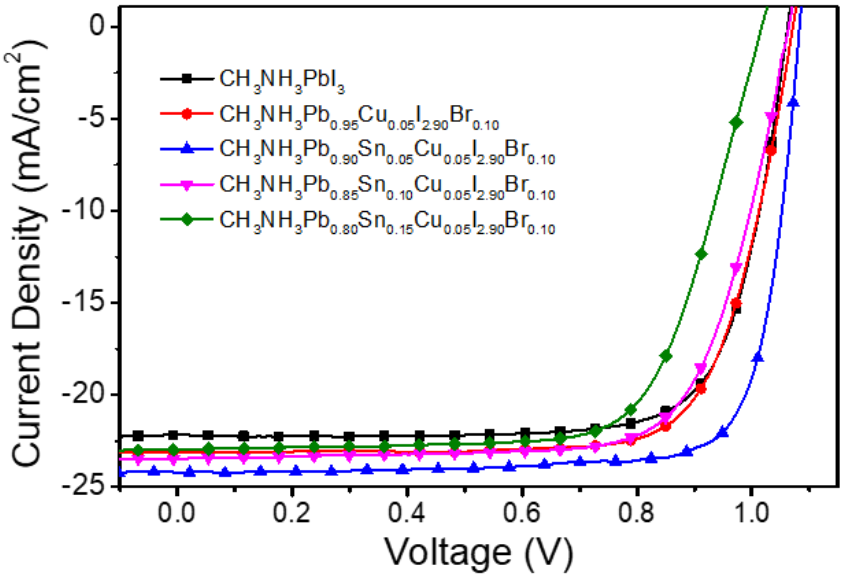

Figure S13. *J-V* curve of PSCs with various composition of Pb, Sn and Cu.

Table S4. Cell parameters of PSCs with various composition of Pb, Sn and Cu.

Perovskite Layer	J_{SC} (mA cm^{-2})	V_{OC} (V)	FF	PCE (%)
$MAPbI_3$	22.18	1.07	0.75	17.89
$MAPb_{0.95}Cu_{0.05}I_{2.90}Br_{0.10}$	23.11	1.08	0.74	18.49
$MAPb_{0.90}Sn_{0.05}Cu_{0.05}I_{2.90}Br_{0.10}$	23.97	1.08	0.81	21.08
$MAPb_{0.85}Sn_{0.10}Cu_{0.05}I_{2.90}Br_{0.10}$	23.48	1.07	0.72	18.05
$MAPb_{0.80}Sn_{0.15}$ $Cu_{0.05}I_{2.90}Br_{0.10}$	22.99	1.03	0.70	16.45

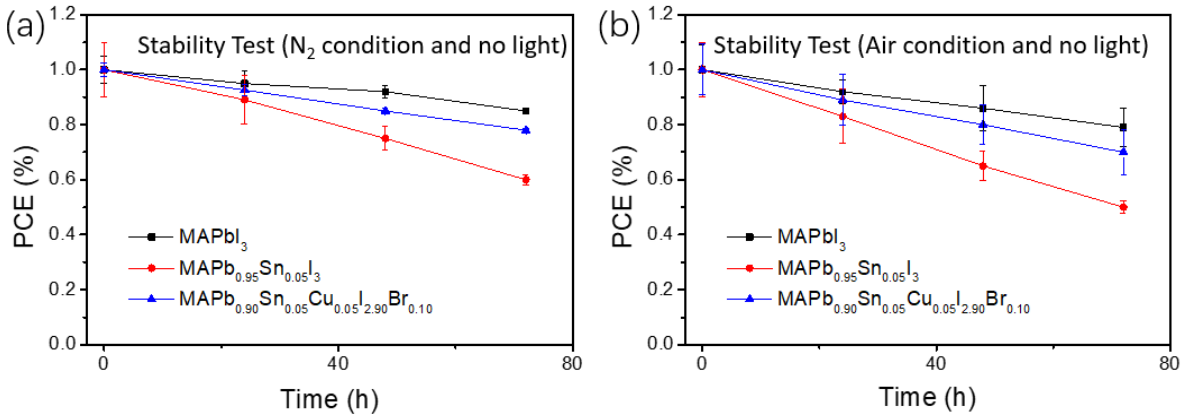

Figure S14. Stability tests of perovskite solar cells in (a) N_2 and (b) air conditions.